



Trans. Nonferrous Met. Soc. China 32(2022) 1948-1960

Transactions of Nonferrous Metals Society of China

www.tnmsc.cn



Densification and grain growth kinetics of boron carbide powder during ultrahigh temperature spark plasma sintering

Mei ZHANG¹, Wen-jun WANG^{1,2}, Tie-chui YUAN¹, Si-yao XIE³, Rui-di LI¹, Zhi-hui ZHOU¹, Yun-bao XU⁴

- 1. Science and Technology on High Strength Structural Materials Laboratory, State Key Laboratory of Powder Metallurgy, Central South University, Changsha 410083, China;
 - 2. Zhejiang Libo Industrial Co., Ltd., Shaoxing 312000, China;
- 3. School of Materials Science and Engineering, Hefei University of Technology, Hefei 230009, China;
 - 4. Hunan Institute of Engineering, Xiangtan 411100, China

Received 20 January 2022; accepted 27 May 2022

Abstract: Dense B₄C material was fabricated using spark plasma sintering (SPS), and the densification mechanisms and grain growth kinetics were revealed. The density, hardness, transverse flexure strength and toughness of samples were investigated and the model predictions were confirmed by SEM and TEM experimental observations. Results show that SPSed B₄C exhibits two sintering periods: a densification period (1800–2000 °C) and a grain growth period (2100–2200 °C). Based on steady-state creep model, densification proceeds by grain boundary sliding and then dislocation-climb-controlled mechanism. Grain growth mechanism is controlled by grain boundary diffusion at 2100 °C, and then governed by volume or liquid-phase diffusion at 2200 °C.

Key words: boron carbide; spark plasma sintering; densification mechanism; grain growth mechanism; grain boundary; diffusion

1 Introduction

Boron carbide (B₄C) has been used in high technology industries like armors, high temperature thermoelectric conversion and aerospace gyroscope bearing owing to its low density, high hardness and good friction and wear resistance. However, the difficulty in obtaining dense B₄C ceramics limits their further applications [1–5], due to the strong covalent bonds of B—C and the low self-diffusion coefficient [3,6–8]. Several theoretical and experimental studies [7–12] have suggested that the addition of sintering aids could promote densification, but the second phase formation and grain growth would degrade mechanical properties or even cause catastrophic failures of products. To

obtain sufficient densification with limited grain growth, pressure-assisted sintering, the spark plasma sintering (SPS) was generally highlighted in previous research for shaping high dense B₄C material with small grain size, and many efforts have been made revealing the mechanisms behind [13-18]. For example, ZHANG et al [19] investigated the thermal and stress fields during densification in the temperature range without grain growth, and found that deformation controlled by grain-boundary diffusion dominant densification mechanism. MOSHTAGHIOUN et al [7] consolidated B₄C under pulse electric current and used intense twin-detwinning formation to validate exotic grain growth following Bose-Einstein law. CHAUHAN et al [20] found that the grain sizes increased with

boron doping in boron carbide under the identical sintering conditions. Traditionally, grain growth and densification are two competing processes in sintering. Abnormal grain growth occurs in B₄C together with sacrifice of peripheral small grains, and deleteriously acts as a defect source for mechanical properties [21–23]. Therefore, the exact mechanisms favoring densification and restraining grain growth remain a systematic clarification.

Currently, the research of SPSed B₄C sintered above 2200 °C was limited due to the high radial temperature gradient inside during the high-temperature stage. The effect of electric current and stress will make the powder partially melt and cause abnormal grain growth, and the dominant mechanism is different from that of uniform heat transfer condition. Therefore, we chose a more suitable size of die to further increase the sintering temperature to 2200 °C to reveal the grain growth mechanisms involved. The grain growth and densification behaviors were investigated via both the experimental observations and modelling.

2 Experimental

2.1 Characterization of raw powder

High purity B₄C powders were used in this work with a chemical composition (wt.%) of O 2.4, Fe 0.11, B 77.86 and C 19.53. B₄C powders were washed with concentrated hydrochloric acid and then sedimentated with deionized water. The particle size distribution of washed powders was detected by laser diffraction particle size analysis dispersed by alcohol and the microstructure was observed bv scanning electron microscopy (NOVATM NanoSEM230, Holland), which are shown in Fig. 1. The washed powders consisted of irregular granules with an average particle size of around 2 µm and all the particles were less than 10 μm.

2.2 Sintering

The prepared B₄C powders were sintered in an SPS apparatus with FCT SPS system (GmbhGEwerbepark 16 96528, Germany). The powder was weighed to 9 g and then placed in a d 30 mm (internal diameter) graphite module which had been lined with a thick graphitic sheet previously for easy mold release after sintering. The macroscopic applied pressure was fixed at 40 MPa

and heating rate were fixed at 100 °C/min. For densification analysis, soaking time of 20 min and soaking temperature range of 1800–2200 °C were chosen, and for grain growth analysis, different soaking time of 1,5, 10, 20, 60 min at soaking temperature of 2100 and 2200 °C was chosen. During the sintering procedures, the temperature was measured by an optical pyrometer focused on the outer surface of the graphite die. Some steps, such as heating, soaking and cooling procedures, were conducted in vacuum at 10⁻² Pa.

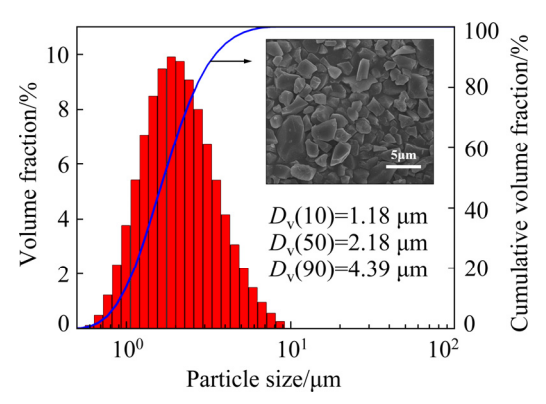


Fig. 1 Particle size distribution and SEM image of washed lab-made B₄C powder

Throughout the tests, instantaneous sintering data including temperature, pressure, and displacement of the uppiston, were recorded by the system [24]. To deduce the thermal expansion contributions from the graphite die and apparatus, a set of blank experiments were conducted under the same conditions. The instantaneous sample height variation and its instantaneous relative density were correlated as follows:

$$D = \left(\frac{L_{\rm f}}{L}\right) D_{\rm f} \tag{1}$$

where D is the instantaneous relative density, $D_{\rm f}$ is the final relative density of the sintered sample, L is the height of the powder bed and $L_{\rm f}$ is the final height of the sample.

2.3 Material characterization

The apparent densities of the samples were measured by the Archimedes method in deionized water at least 5 times for each sample. The relative density $D_{\rm f}$ was obtained using a B₄C theoretical density of 2.52 g/cm³.

All the samples were polished by diamond powders and then electrolytically etched in 10%

NaOH solution with a voltage of 25 V for 6 s. Microstructures of the polished samples were observed bv scanning electron microscopy NanoSEM Holland) (NOVATM 230, metallographic microscopy (OM, Leica DM2700P, Germany). For each sample, the average grain size was determined by line-intercept method, in which at least 150 grains from SEM and metallograph images of the polished surface were considered. Thin foils of fully dense samples were prepared by ion milling and the detailed microstructures were observed by transmission electron microscopy (Tecnai G2 F20 S-TWIN, FEI, USA).

All the samples were cut into specific shapes by wire electrical discharge machining to test the mechanical properties. The transverse flexure strength of the bars with sizes of 3 mm \times 4 mm \times 20 mm was obtained by the three-point rupture method with a span length of 14.5 mm, and 3 bars were tested for each sample. Fracture toughness was tested by the single edge notch beam method on bars of 5 mm ×5 mm ×30 mm in size with a span length of 20 mm and notch length of 2.5 mm. The strength and toughness tests were applied at room temperature using an electronic universal testing machine (Instron-3369, USA) with a loading speed of 5 m/s. The samples for microhardness tests were polished with a 1 µm diamond suspension and then measured by a hardness tester (MICROMET 5104, Changsha, China) with a load of 500 g at room temperature, each sample was tested at more than 15 points, from the center to the edge of the sample and the average values were taken.

3 Results

Figure 2 shows that the relative density and the densification rate (1/D)(dD/dt) (t is the time) vary with sintering temperature during powder sintering at 2200 °C, which is also the maximum stable operating temperature of this SPS apparatus. The starting density of the compaction was measured to be 57% when an applied pressure of 40 MPa was imposed at room temperature for 5 s on the powder bed. At the initial heating stage, the relative density of the sample barely increased, and then it increased rapidly after an onset temperature $T_{\rm d}$, which shows that a full density was achieved after soaking for 20 min at 2200 °C. The densification rate exhibited a clear peak at approximately 2100 °C.

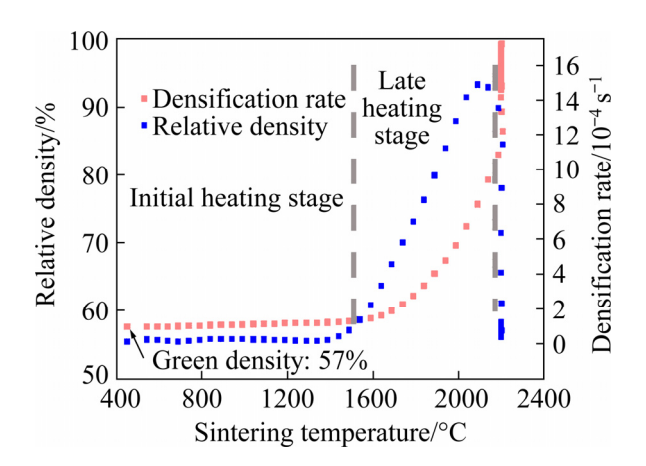


Fig. 2 Densification and densification rate curves of sample sintered at 2200 °C

The continuous instantaneous relative densities of the samples at different soaking temperatures during the whole sintering process are shown in Fig. 3. The morphologies of sintered samples are shown in the bottom right corner. The relative density increased with increasing the sintering temperature, which was similar to that of hot press sintering. However, when the temperature was higher than 2100 °C, the densification curves were remarkably close, indicating that densification cannot be further accelerated by increasing the sintering temperature. The sample sintered at 2200 °C was full of macrocracks and broken after demolding. Samples sintered at 2100 and 2200 °C are almost dense (relative density over 99%), but at 2200 °C, the fine powder partially melted at the grain boundary; as the fine powder (particle size <1 µm) content is less than 10%, there is no significant change in the macroscopic densification curve compared with 2100 °C.

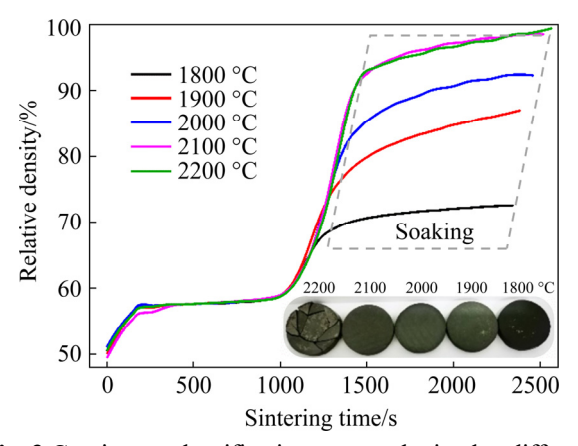


Fig. 3 Continuous densification curves obtained at different SPS temperatures and images of sintered samples

The densification curves during the soaking fixed at 20 min are shown in Fig. 4. Regardless of the sintering temperature, all the curves exhibited similar behavior: accelerated densification at the beginning of the soaking stage and then stabilization at the rest of the soaking time. At the beginning of the soaking stage, a higher soaking temperature led to a higher relative density and faster densification rate, except in the temperature range of 2100–2200 °C.

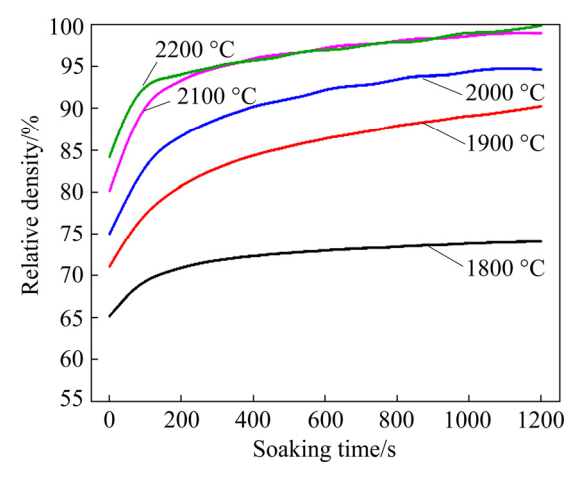


Fig. 4 Densification curves obtained in function of soak time

Figure 5 shows the grain characteristics of the polished and etched samples sintered at 1800–2200 °C for 20 min. Figure 6 reveals the grain size and relative density varying with the sintering temperature of samples when soaking for 20 min. At 1800–2000 °C, the relative density increased with the temperature, and the grain size remained unchanged. When the temperature reached 2100 °C, the relative density increased to higher than 99%, and grain growth occurred at that time.

The densification behavior has a significant effect on the mechanical properties. The transverse flexure strength, fracture toughness and hardness of B₄C sintered at different temperatures are shown in Fig. 7. The results showed that the hardness increased with the relative density regardless of the grain size, whereas the strength was significantly affected by the grain size. The sample sintered at 2000 °C had a lower density but a higher strength and toughness than those sintered at 2100 °C. Finer grains have abundant grain boundaries that can absorb more energy in resistance to deformation.

It was obvious that by selecting a proper soaking temperature and time, it is obvious that

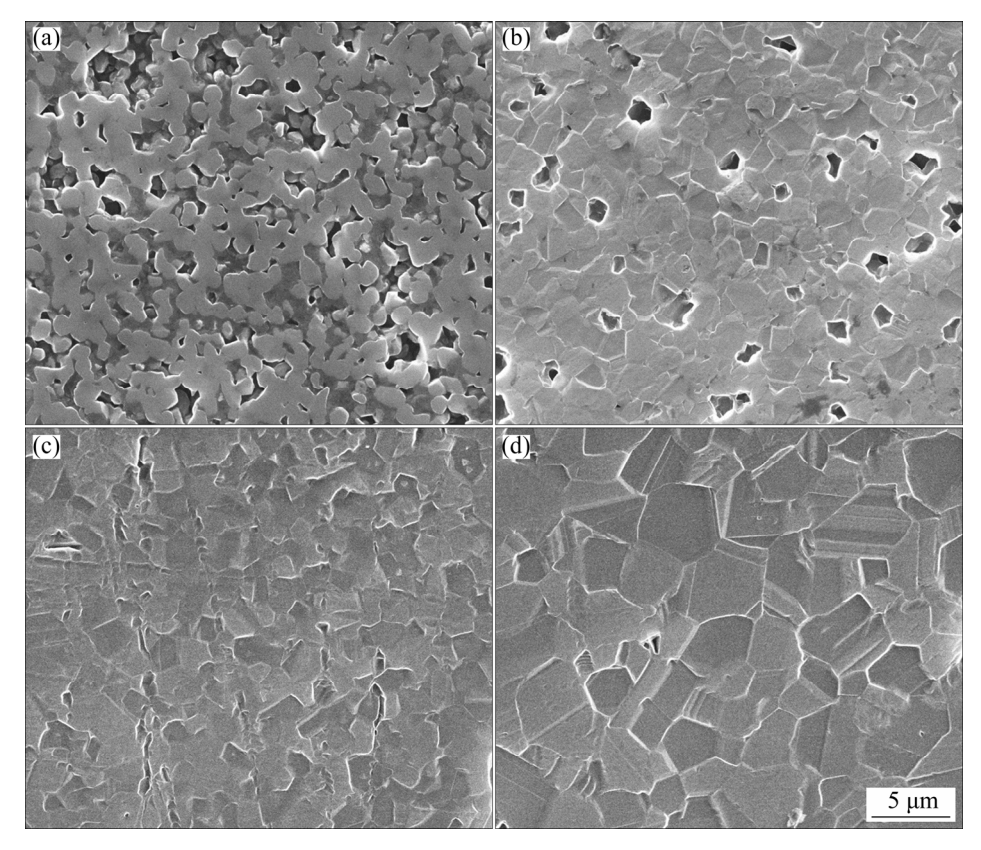


Fig. 5 SEM images of polished and etched samples sintered at different SPS temperatures for 20 min: (a) 1800 °C; (b) 1900 °C; (c) 2000 °C; (d) 2200 °C

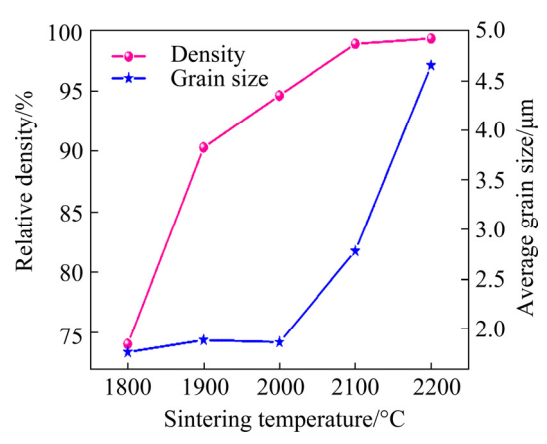


Fig. 6 Grain size and relative density of sample obtained by SPS with soaking time of 20 min

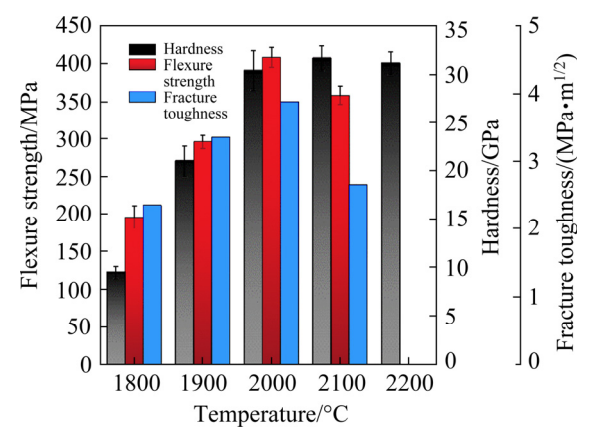


Fig. 7 Effect of soaking temperature on mechanical properties of sintered B₄C

dense B_4C ceramic with a relative density over 99% can be obtained with excellent mechanical properties. The grain size limited to the submicron level (2 μ m) without any growth at all can be obtained in the same way. In this case, the grain size is very similar to the average particle size of the raw powder.

Figure reveals the typical fracture morphologies of the samples sintered at different soaking temperatures. As shown in the SEM images, open pores existed in the sample sintered at 1800 °C, and the main fracture mode was intergranular fracture. Only closed pores could be found when the temperature increased to 2000 °C. Fully dense bulks were fabricated at 2100 °C, and the fracture turned to the transgranular mode. However, as the temperature increased to 2200 °C, the overheated temperature melted some boundaries of small grains. Two distinguished areas, marked as A and B, could be found from the macroscopic fracture surface at the bottom-right corner of Fig. 8(e). Zone A corresponded to the large-grain region (Fig. 8(e)), and Zone B corresponded to the fine grain region (Fig. 8(f)). According to Fig. 1, B₄C powders had about 10% particle less than 1 μm. The finer the powder size was, the higher the surface activation energy was. With the radial stress, fine powders mainly distributed among

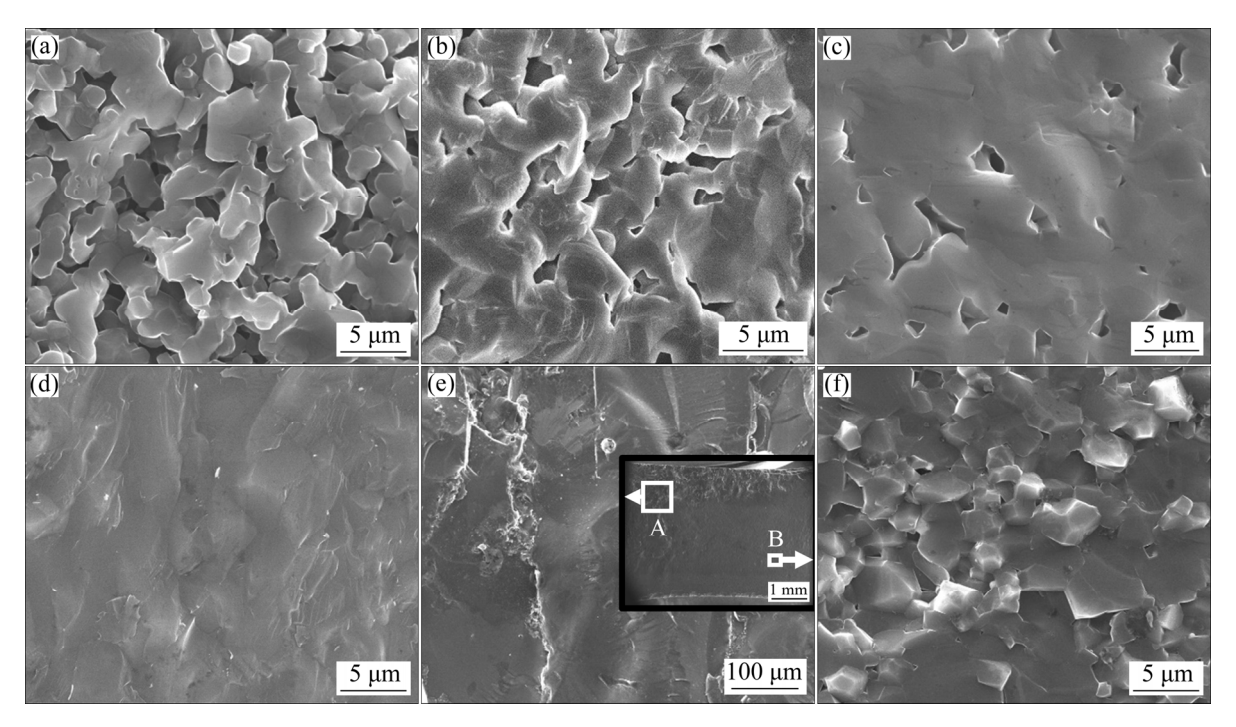


Fig. 8 Fracture surface morphologies of sintered B₄C at different soaking temperatures: (a) 1800 °C; (b) 1900 °C; (c) 2000 °C; (d) 2100 °C; (e) Large grain area (Zone A) of 2200 °C; (f) Fine grain area (Zone B) of 2200 °C

coarse particles. At high soaking temperature, the surface of fine powder melted and stuck to the coarse particles, which impede the formation of the sintering necks, thus leading to the reduction of grain boundary strength. The fracture surface exhibited typically intergranular characteristics due to the decrease in grain boundary bonding strength caused by high soaking temperature.

4 Discussion

4.1 Densification kinetics without grain growth

For the high-temperature pressure-assisted sintering during the isothermal stage, atomic matter migration can be treated as steady-state creep strain, and a creep analytical model based on that has been used to understand the densification mechanism. For ceramics, the kinetic equation can be written in a simplified version by dropping the negligible electromigration, which can be described as [25]

$$\dot{\varepsilon} = \frac{1}{D} \frac{\mathrm{d}D}{\mathrm{d}t} = \frac{A\Phi\mu_{\mathrm{eff}}b}{kT} \left(\frac{b}{G}\right)^p \left(\frac{\sigma_{\mathrm{eff}}}{\mu_{\mathrm{eff}}}\right)^n \tag{2}$$

where $\dot{\varepsilon}$ is the creep rate, A is a constant, Φ is the diffusion coefficient, $\mu_{\rm eff}$ is the instantaneous effective shear modulus, which varies with the internal porosity, b is the magnitude of Burgers vector, k is the Boltzmann constant, T is the thermodynamic temperature, G is the grain size, $\sigma_{\rm eff}$ is the instantaneous effective pressure acting on the powder bed, p is the grain size exponent and p is the stress exponent.

According to HILLERT [26], powders are assumed to be single-sized spheres close to random dense stacking. It can be seen from Fig. 1 that B₄C powders are polyhedral granules, and the initial distribution follows a lognormal distribution in a narrow size range. By introducing a three-dimensional shape-size correction factor determined to be 1.2 [25], the instantaneous pressure is equal to the following equation:

$$\sigma_{\text{eff}} = 1.2 \times \frac{1 - D_0}{D^2 (D - D_0)} \sigma_{\text{mac}}$$
(3)

where σ_{mac} is the macroscopic compaction pressure (40 MPa) applied to the powder bed (B₄C) and D_0 is the starting green density.

It is proposed that the elastic modulus of porous materials during sintering depends on the instantaneous porosity of the sample as [25]

$$\mu_{\text{eff}} = \frac{E_{\text{th}}}{2(1+v)} \frac{D - D_0}{1 - D_0} \tag{4}$$

where $E_{\rm th}$ and v are the elastic modulus and Poisson's ratio of theoretically dense material, respectively. For B₄C, $\mu_{\rm eff}$ can be determined by taking $E_{\rm th}$ equal to 470 GPa [19] and v equal to 0.18 [19]. Sintering densification kinetics (Eq. (2)) can be written as follows, by taking Eqs. (3) and (4) into consideration:

$$\frac{1}{\mu_{\text{eff}}} \frac{1}{D} \frac{dD}{dt} = K_0 \frac{\exp[-Q_d/(RT)]}{T} \left(\frac{\sigma_{\text{eff}}}{\mu_{\text{eff}}}\right)^n \tag{5}$$

where $K_0 (= Bb\Phi_0/k)$ is a constant with Φ_0 being the pre-exponential factor of Φ and B a constant, Ris the molar gas constant and Q_d is the apparent activation energy of the mechanism controlling densification. The densification mechanism of the SPS experiments can be interpreted based on the pressure exponent n, the sintering activation energy Q_d and the grain size exponent p according to Eq. (5). The isothermal stage (20 min soaking time) was investigated to evaluate the key densification parameters.

Figure 6 shows that the grain size remained steady at approximately 2 μ m in the temperature range of 1800–2000 °C. By assuming that the grain size was constant when the temperature was in this temperature range or the relative density was below 90% at 2100 and 2200 °C, the grain growth contribution to densification could be neglected. For a fixed temperature, the pressure exponent n can be calculated by transforming Eq. (5) into its logarithmic form as follows:

$$\ln\left(\frac{1}{\mu_{\text{eff}}} \frac{1}{D} \frac{\text{d}D}{\text{d}t}\right) = n \ln\left(\frac{\sigma_{\text{eff}}}{\mu_{\text{eff}}}\right) + K_1 \tag{6}$$

where K_1 is the balancing constant. During the soaking in the temperature range of 1800-2200 °C, it is then possible to have access to the continuous variations of $(1/\mu_{\text{eff}})(1/D)(dD/dt)$ as a function of $\sigma_{\text{eff}}/\mu_{\text{eff}}$; such a representation in logarithmic form is shown in Fig. 9. The slopes of the straight lines are equal to the values of pressure exponent n for different temperatures. It is obvious that n exhibits different values for different soaking stages and temperatures. At this point, it appears that more

than two different mechanisms may be involved for the control of densification during SPS of submicron B₄C powders selected. Regardless of the sintering temperature, at the initial stage, the nvalues are approximately 1, which belongs to low effective stress exponent regime. In the final stage, when the soaking temperature is 1800, 1900, 2000 and 2100 °C, n is equal to 4.6, 2.5, 3.2 and 5.7, respectively, which belong to high effective stress exponent regimes. Finally, when the soaking temperature is 2200 °C, n approaches to 10. It should be noted that at a much higher temperature, n values cannot be calculated by this model because of the apparent grain growth. Moreover, the final sintering stage is reached too early under isothermal conditions, and the soaking time is too short to analyze the n value. The mechanisms during the grain growth stage are analyzed in Section 4.2.

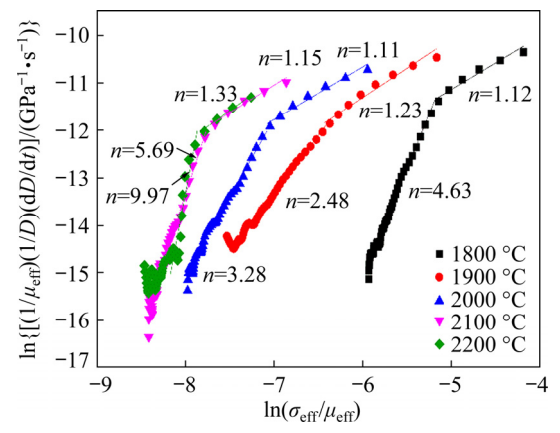


Fig. 9 Effective stress exponent calculated with Eq. (6) in SPS temperature range of 1800–2200 °C and soaking time of 20 min

With the *n* values determined, Eq. (5) can be transformed as follows, which provides the basis for further calculating Q_d :

$$\ln \left[\frac{T}{\mu_{\text{eff}}} \left(\frac{\mu_{\text{eff}}}{\sigma_{\text{eff}}} \right)^n \frac{1}{D} \frac{dD}{dt} \right] = -\frac{Q_d}{RT} + K_2$$
(7)

where K_2 is a constant. Therefore, the slope of the straight line obtained when drawing Eq. (7) corresponds to the value of $-Q_d/R$.

Figure 10 shows the variation in the densification rate as a function of D. The value of (1/D)(dD/dt), which belonged to the initial stage, was chosen to be $7.5\times10^{-4}\,\mathrm{s}^{-1}$. Then, the corresponding $\sigma_{\rm eff}$ and $\mu_{\rm eff}$ for a certain relative density can be calculated using Eqs. (3) and (4).

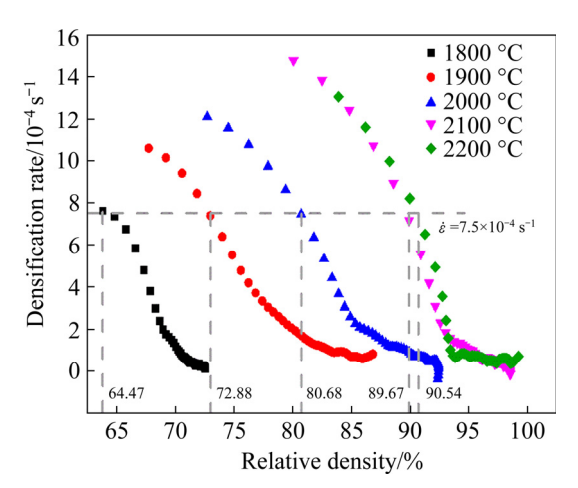


Fig. 10 Fixed value of densification rate chosen at initial densification stage

With the effective pressure and shear modulus, numerical spots of Eq. (7) at different temperatures and the linear fitting line are shown in Fig. 11. The Q_d of (330.95±49.66) kJ/mol is finally calculated.

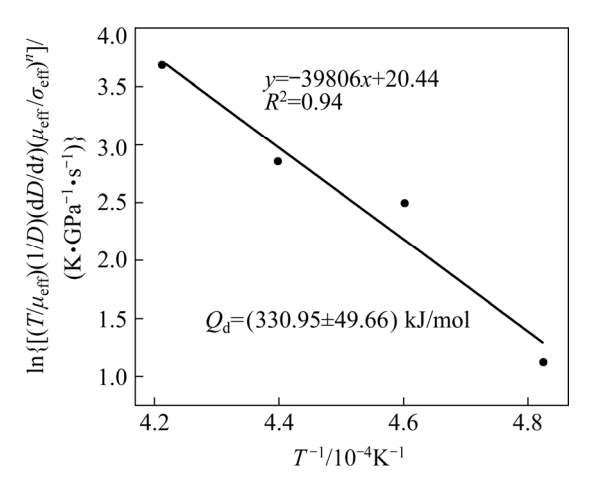


Fig. 11 Apparent activation energy of densification of B₄C

Some quantitative investigations have been performed on creep and carbon atom diffusion in boron carbides. ABZIANIDZE et al [27] has demonstrated that carbon atoms were the slowest atoms during atom diffusion of boron and carbon in B₄C ceramics. The diffusion activation energy of carbon in B₄C is 382 kJ/mol, which is close to the sintering apparent activation energy of 330 kJ/mol acquired in the present work. MOSHTAGHIOUN et al [16] performed creep test of pure dense B₄C under 250 MPa and the activation energy *Q* was 632 kJ/mol. The stress is much higher than that in current work, which can explain the difference in the energy. SKOROKHOD [28] sintered B₄C

ceramics (average particle size of 0.63 mm) without pressure and calculated the activation energy of 717 kJ/mol. EBRAHIMI et al [29] also sintered fine B_4C powders (<2 μ m) using pressureless sintering and calculated an activation energy of (660±20) kJ/mol. The higher activation energy of pressureless sintering compared with that of SPS is due to the absence of pressure and an electric field.

In previous work [19], pure B₄C powders were sintered in a graphite die with a diameter of 40 mm, and the stress exponent during the initial period of soaking time was approximately 2, which corresponded to the densification governed by grain-boundary sliding. With HEA as the sintering aid [30], the stress exponent n approached to 1 and then the densification mechanisms may be controlled by grain-boundary sliding accompanied by interface reaction or lattice diffusion. The apparent activation energy calculated in the current work is close to the carbon atom diffusion activation energy in B₄C, as mentioned above. Therefore, we propose that densification by SPS proceeds by grain boundary sliding accommodated by carbon atom diffusion.

Nevertheless, when the stress exponent value is higher than 3, it always represents a dislocation motion mechanism. According to the dislocation climb theory proposed by WEERTMAN [31], the creep rate controlled by dislocation climbing ($\dot{\varepsilon}_{\rm DC}$) has the following expression:

$$\dot{\varepsilon}_{\rm DC} = \frac{b}{6d^3 \sqrt{\pi Md}} V_{\rm m} \tag{8}$$

where d is the distance between neighboring plane spacings emitting the involved dislocations (according to Poirier's study, $d=\beta\mu b/\sigma$ and β is a constant), M is the dislocation source density and $V_{\rm m}$ is the climbing rate. During the high temperature sintering, the dislocation climbing rate can be expressed by [31]

$$V_{\rm m} = \frac{\phi_{\rm v} \sigma b^3}{b k T} \tag{9}$$

where ϕ_v is the volume diffusion coefficient of vacancies

By incorporating Eq. (8) into Eq. (7), the creep densification rate may be derived:

$$\dot{\varepsilon}_{DC} = K_3 \frac{\phi_{v}}{6b^{3.5} \sqrt{M}} \left(\frac{\sigma}{\mu}\right)^{4.5} \frac{\mu b^3}{kT}$$
 (10)

where K_3 is a constant. If M is independent of the applied pressure, then Eq. (5) can be adapted as follows:

$$\frac{1}{\mu_{\text{eff}}} \frac{1}{D} \frac{dD}{dt} = K_4 \left(\frac{\sigma_{\text{eff}}}{\mu_{\text{eff}}} \right)^{4.5} \frac{\exp[-Q_d/(RT)]}{T}$$
 (11)

where K_4 is a constant.

Conversely, if M depends on effective stress, then the relation between M and σ may be [24]

$$M \propto d^{-3} = \left(\frac{\sigma}{\mu b}\right)^3 \tag{12}$$

Then, Eq. (11) can be adaptable as follows:

$$\frac{1}{\mu_{\text{eff}}} \frac{1}{D} \frac{dD}{dt} = K_5 \left(\frac{\sigma_{\text{eff}}}{\mu_{\text{eff}}} \right)^3 \frac{\exp[-Q_d/(RT)]}{T}$$
 (13)

where K_5 is a constant.

As shown in Fig. 9, when the soaking temperature was 1800–2000 °C, the stress exponent value was approximately 3 or 4.5. At this point, even if the corresponding apparent activation energy has not been determined, we propose that during the final densification in the temperature range of 1800–2000 °C, the densification of SPS proceeds by a dislocation-climb-controlled mechanism. At 1800 °C, the dislocation source is independent of the effective stress, but with increasing temperature, the dislocation source density tends to depend on the effective stress.

To confirm the dislocation-climb densification mechanism, TEM observations of sintered samples were performed, as shown in Fig. 12. As shown from Figs. 12(a-c), all samples have dislocations, and a complicated network of dislocations inside the top right B₄C grain can be found, which corresponds to dislocation climbing and entanglement. Usually, dislocation line the emanating from the grain boundary ends within the grain in the form of a dislocation loop [31]. A grain boundary HRTEM image with SAED patterns of the sample sintered at 2100 °C are shown in Fig. 12(d). Amorphization takes place at the edge, resulting in plastic deformation of B₄C. Therefore, the densification mechanism at this stage is dominated by high-temperature plastic deformation controlled by dislocation climbing. When the temperature is extremely high (2200 °C), accompanied by high effective stress, twin bands inside B₄C are found (Fig. 12(e)). Twins usually

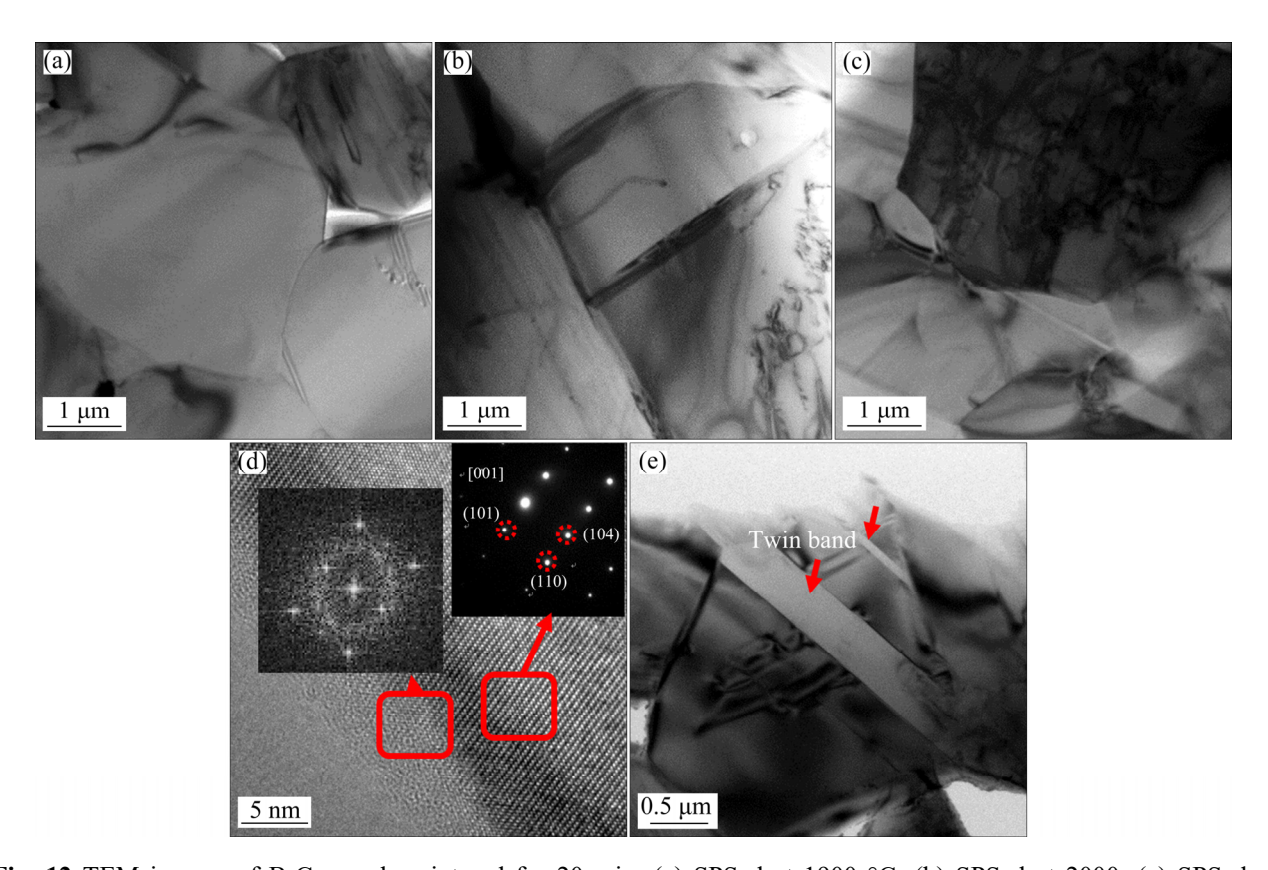


Fig. 12 TEM images of B_4C samples sintered for 20 min: (a) SPSed at 1900 °C; (b) SPSed at 2000; (c) SPSed at 2100 °C; (d) HRTEM image of grain boundary in sample SPSed at 2100 °C; (e) SPSed at 2200 °C

both start and end at the grain boundaries, excess energy of the system is released through twin formation and grain growth, and the grain growth mechanism is then investigated.

The crystal structure of B₄C is a rhombohedral unit consisting of a 12-atom icosahedral structure with a 3-atom chain, and slip can occur on more than one slip systems [20]. Dislocations circumvent obstacles by climbing over them through the creation or destruction of vacancies or interstitials. When dislocations are piled up in groups, their stress field induces dislocations on a second slip system to move to the group. After an external stress is applied, many dislocation loops are produced from a Frank-Read source, which move until they are stopped by some natural obstacles such as grain boundary. In rhombohedral structures, a dislocation line may split up into half dislocations with a stacking fault between them. Figure 13 shows how dislocations appear and expand along the (104) lattice plane, as revealed in the HRTEM image. The basic interplanar crystal distance along (104), which is magnified in Fig. 13(b), is approximately 0.2541 nm, the angle to (021) is approximately 63.66°, dislocation expansion from the top, is magnified in Fig. 13(d), and the interplanar spacing narrows to 0.2429 nm. Figures 13(c-e) show the distortion of the lattice due to dislocation climbing. The distance in the (104) lattice plane and the angle to (021) change to 0.2489 nm and 66.98°, respectively.

To determine the dislocation density of sintered bulks, XRD analysis of samples sintered at different temperatures were revealed, and the dislocation density of the samples was calculated by modified Williamson–Hall method, which can be shown as follows according to UNGÁR and BORBÉLY [32]:

$$\Delta K = \frac{0.9}{G} + \left(\frac{\pi C_{R} b^{2}}{2}\right)^{1/2} \rho_{d}^{1/2} \left(K \overline{C}^{1/2}\right) + N$$
 (14)

where ΔK is the value of the full width at half maximum (FWHM), C_R is a parameter determined by the effective outer cutoff radius of dislocation, b is around 5.17 Å for B₄C [33], ρ_d is the dislocation density, $K=2\sin\theta/\lambda$ (θ is the diffraction angle and λ is the wavelength of X-ray), C is the dislocation

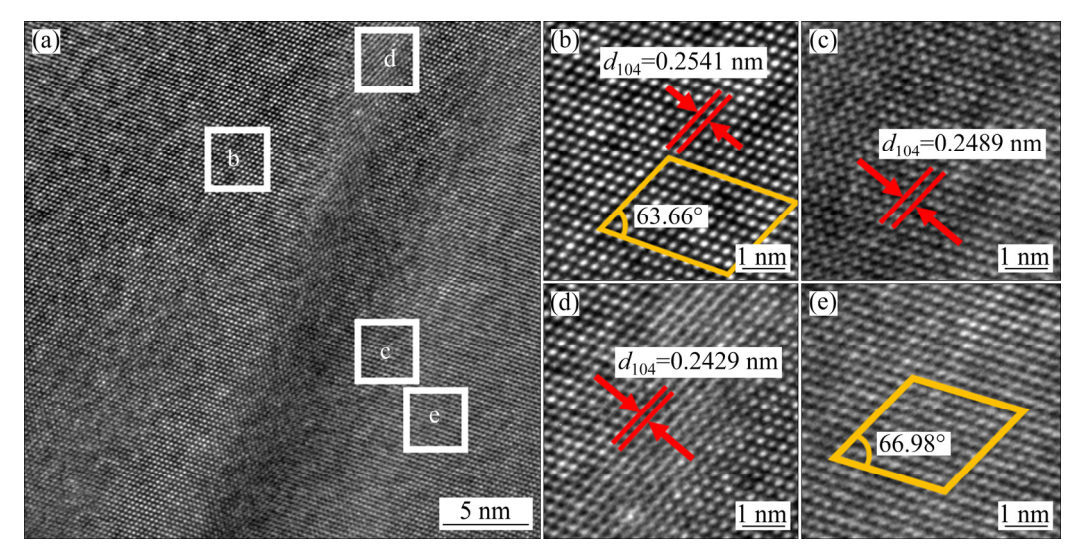


Fig. 13 HRTEM image of dislocation climbing in B₄C sintered at 2100 °C (a) and magnified HRTEM image of specific area (b-e)

control factor, and N is constant. According to Eq. (14), the slope of the straight line obtained when drawing $\Delta K = f(K\overline{C}^{1/2})$ corresponds to the value of $(\pi C_R b^2/2)^{1/2} \rho_d^{1/2}$. With the values of band C_R [33], the dislocation density of the sample can be determined. Figure 14 shows XRD patterns of the samples, and the magnified diffraction peaks of (021) are revealed in Fig. 14(b). The peaks are slightly shifted to the left due to the residual stress compared to the standard values. The slopes of Williamson-Hall plots of samples and the corresponding dislocation density are marked in Fig. 14(c). Results revealed that the dislocation density of the sample sintered at low temperature is less than that at high temperature in the temperature range of 1800-2000 °C, while it fluctuates when the temperature is higher than 2000 °C due to grain growth. Figure 2 shows densification rate peaks at around 2000 °C, and Fig. 7 shows that sample sintered at 2000 °C has a higher flexure strength, which all results in the acceleration of densification and strengthening by dislocation motion.

4.2 Grain growth mechanism

The isothermal grain size exponent *p* was determined to throw light on the grain growth mechanisms. This was done at 2100 and 2200 °C, with 2100 °C being the temperature at which grain growth is obvious. The grain growth mechanisms of B₄C were revealed using the classical grain growth power law [24]:

$$G^p - G_0^p = K_G t \tag{15}$$

where G_0 is the initial average grain size calculated at different soaking time t, respectively, and K_G is related to the grain growth coefficient.

To exclude the influence of the heating stage on grain growth, we chose the average grain size of the samples after soaking for 1 min to be the initial size. Different p values correspond to different mechanisms [34], with 2, 3 and 4 usually related to grain boundary diffusion, volume or liquid-phase diffusion and surface diffusion, respectively. For p=4, grain growth is controlled by surface diffusion, whereas dense bulks are usually achieved in this temperature range, and free surfaces are rarely provided to the diffusion. Figure 15 shows the plots of Eq. (15) at 2100 and 2200 °C for p values of 1-3. Regression coefficients R^2 are marked around the fitted lines. For 2100 °C, p=2 is acceptable and for 2200 °C, p=3 is more accurate. At the initial grain growth stage at 2100 °C, sufficient sintering necks are provided to facilitate grain boundary diffusion because of high relative density and fine grains, and the grain growth mechanism at this temperature is therefore controlled by grain boundary diffusion. When the temperature reached 2200 °C, the results shown in Fig. 8(e) revealed that partial melting occurred at the grain boundaries, which provided a way for volume diffusion or liquid diffusion. Then, reasonably in this stage, the grain growth mechanism is governed by volume or liquid-phase diffusion.

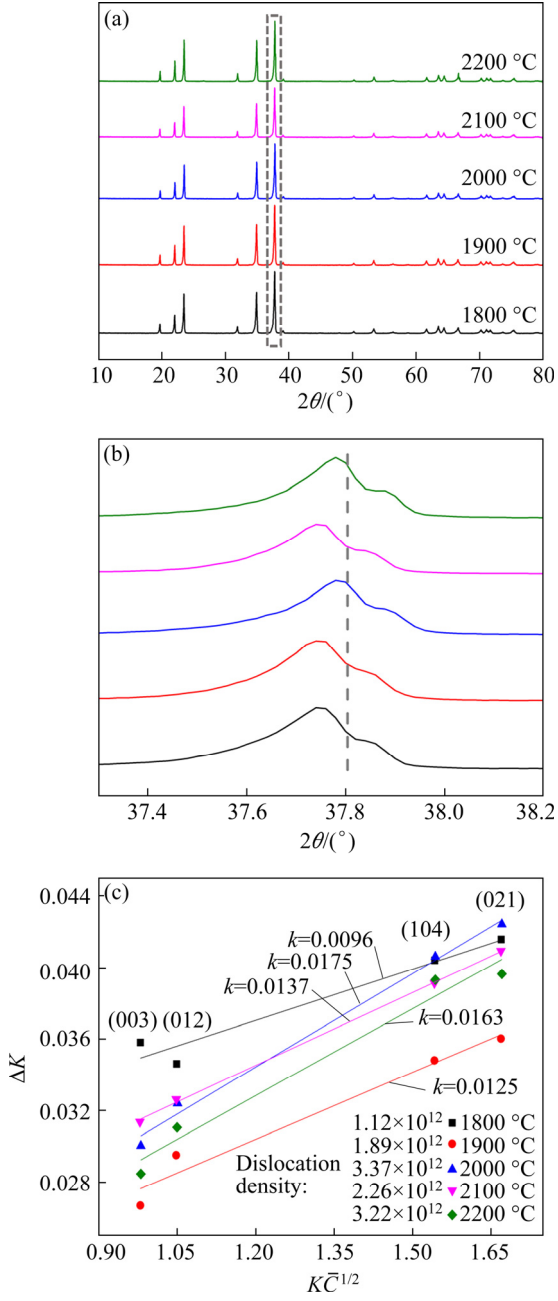


Fig. 14 XRD patterns of B_4C (a), magnified diffraction peak of (021) (b), and dislocation densities of samples calculated by Williamson–Hall method (k is slope of fit line) (c)

5 Conclusions

(1) Two separate sintering periods during densification are shown: densification with a constant grain size in the temperature range of 1800–2000 °C and grain growth without apparent densification in the temperature range of 2100–2200 °C. In the densification regime, two distinct stages corresponding to two different mechanisms were involved based on different

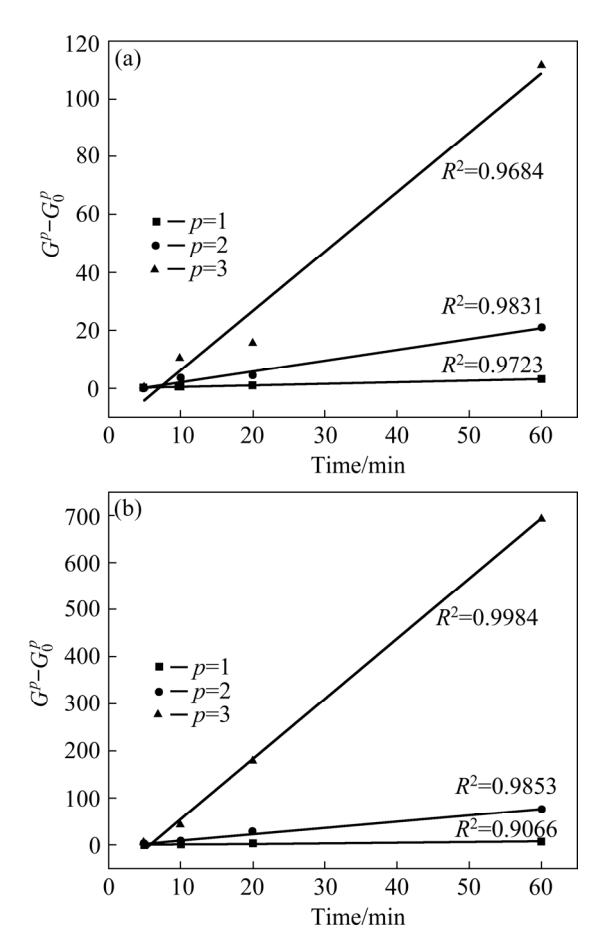


Fig. 15 Plots of Eq. (15) for different values of grain size exponent p: (a) 2100 °C; (b) 2200 °C

effective stress exponents n: in the initial stage, which belongs to low effective stress exponent regime, $n\approx 1$, the densification by SPS proceeds by grain boundary sliding accommodated by carbon atom diffusion, and the apparent sintering activation energy $Q_{\rm d}$ of (330.95 ± 49.66) kJ/mol is finally calculated; in the final stage, which belongs to the high effective stress exponent regime, n>3, and the densification of SPS proceeds by a dislocation-climb-controlled mechanism.

(2) When the temperature exceeds 2100 °C, the grain growth kinetics of B₄C was investigated using grain growth power law. The results indicate that at the initial grain growth stage at 2100 °C, the mechanism involved is controlled by grain boundary diffusion, and when the temperature reaches 2200 °C, the grain growth mechanism is governed by volume or liquid-phase diffusion.

Acknowledgments

The authors wish to acknowledge the financial supports from the National Natural Science

Foundation of China (No. 51874369) and Hunan Provincial Natural Science Foundation, China (No. 2021JJ30856). Mei ZHANG gratefully acknowledges the China Scholarship Council for financial supports (No. CSC201906370123) and the Fundamental Research Funds for the Central Universities of Central South University, China (No. 2020zzts084).

References

- [1] ZHAO S, LI B, REMINGTON B A, WEHRENBERG C E, PARK H S, HAHN E N, MEYERS M A. Directional amorphization of covalently-bonded solids: A generalized deformation mechanism in extreme loading [J]. Materials Today, 2021, 49: 59–67.
- [2] CHEN Lei-lei, ZHANG Zhen-yu, WANG Ji, LOU Ming, CHEN Xiao-long, YUAN Yuan, WANG Lu, XU Kai, CHANG Ke-ke. Rigid three-dimensional networks of hafnium diboride for improving mechanical and wear properties of boron carbide [J]. Materials & Design, 2021, 210: 110069.
- [3] AVCCIOĞLU S, KAYA F, KAYA C. Morphological evolution of boron carbide particles: Sol-gel synthesis of nano/micro B₄C fibers [J]. Ceramics International, 2021, 47: 26651–26667.
- [4] AMIRNASIRI A, MIRSALEHI S E. Investigation of interfacial reactions and wetting behavior of boron carbide by AMS 4777 brazing alloy [J]. Ceramics International, 2021, 47: 34414–34424.
- [5] GUPTA R, NANDA T, PANDEY O P. Comparison of wear behaviour of LM13 Al-Si alloy based composites reinforced with synthetic (B₄C) and natural (ilmenite) ceramic particles [J]. Transactions of Nonferrous Metals Society of China, 2021, 31: 3613-3625.
- [6] CHEN M, MCCAULEY J W, HEMKER K J. Shock-induced localized amorphization in boron carbide [J]. Science, 2003, 299: 1563–1566.
- [7] MOSHTAGHIOUN B M, GÓMEZ-GARCÍA D, RODRÍGUEZ A D. Exotic grain growth law in twinned boron carbide under electric fields [J]. Journal of the European Ceramic Society, 2018, 38: 4590–4596.
- [8] ZHANG Mei, FENG Xiao, YUAN Tie-chui, LI Rui-di. Densification kinetics of boron carbide with medium entropy alloy as a sintering aid during spark plasma sintering [J]. International Journal of Applied Ceramic Technology, 2019, 16: 389–399.
- [9] RAHMANI K, MAJZOOBI G H, EBRAHIM-ZADEH G, KASHFI M. Comprehensive study on quasi-static and dynamic mechanical properties and wear behavior of Mg-B₄C composite compacted at several loading rates through powder metallurgy [J]. Transactions of Nonferrous Metals Society of China, 2021, 31: 371–381.
- [10] THEVENOT F. Boron carbide—A comprehensive review [J]. Journal of the European Ceramic Society, 1990, 6: 205–225.
- [11] DU Xian-wu, ZHANG Zhi-xiao, WANG Yang, WANG Ji-lin, WANG Wei-min, WANG Hao, FU Zheng-yi. Hot-pressing

- kinetics and densification mechanisms of boron carbide [J]. Journal of the American Ceramic Society, 2015, 98: 1400–1406.
- [12] MOSHTAGHIOUN B M, ORTIZ A L, GÓMEZ-GARCÍA D, DOMÍNGUEZ-RODRÍGUEZ A. Densification of B₄C nanopowder with nanograin retention by spark-plasma sintering [J]. Journal of the European Ceramic Society, 2015, 35: 1991–1998.
- [13] ZHANG Cui-ping, RU Hong-qiang, ZONG Hui, SUN Wei-kang, ZHU Jing-hui, WANG Wei, YUE Xin-yan. Coarsening of boron carbide grains during the infiltration of porous boron carbide preforms by molten silicon [J]. Ceramics International, 2016, 42: 18681–18691.
- [14] ROY T K, SUBRAMANIAN C, SURI A K. Pressureless sintering of boron carbide [J]. Ceramics International, 2006, 32: 227–233.
- [15] MOSHTAGHIOUN B M, GARCÍA D G, RODRÍGUEZ A D. High-temperature deformation of fully-dense fine-grained boron carbide ceramics: Experimental facts and modeling [J]. Materials & Design, 2015, 88: 287–293.
- [16] MOSHTAGHIOUN B M, GARCÍA D G, RODRÍGUEZ A D, PADTURE N P. High-temperature creep deformation of coarse-grained boron carbide ceramics [J]. Journal of the European Ceramic Society, 2015, 35: 1423–1429.
- [17] NIE Qiang-qiang, CHEN Guo-hong, WANG Bing, YANG Lei, TANG Wen-ming. Process optimization, microstructures and mechanical/thermal properties of Cu/Invar bi-metal matrix composites fabricated by spark plasma sintering [J]. Transactions of Nonferrous Metals Society of China, 2021, 31: 3050–3062.
- [18] LI Rui-di, NIU Peng-da, YUAN Tie-chui, LI Zhi-ming. Displacive transformation as pathway to prevent micro-cracks induced by thermal stress in additively manufactured strong and ductile high-entropy alloys [J]. Transactions of Nonferrous Metals Society of China, 2021, 31: 1059–1073.
- [19] ZHANG Mei, YUAN Tie-chui, LI Rui-di, XIE Si-yao, WANG Min-bo, WENG Qi-gang. Densification mechanisms and microstructural evolution during spark plasma sintering of boron carbide powders [J]. Ceramics International, 2018, 44: 3571–3579.
- [20] CHAUHAN A, SCHAEFER M C, HABER R A, HEMKER K J. Experimental observations of amorphization in stoichiometric and boron-rich boron carbide [J]. Acta Materialia, 2019, 181: 207–215.
- [21] ZHANG Mei, ZHOU Zhi-hui, YUAN Tie-chui, LI Rui-di, ZHANG Wei-shan, ZHANG Ying-jie. Analysis of abnormal grain growth behavior during hot-press sintering of boron carbide [J]. Ceramics International, 2020, 46: 16345–16353.
- [22] JI Wei, REHMAN S S, WANG Wei-min, WANG Hao, WANG Yu-cheng, ZHANG Jin-yong, ZHANG Fan, FU, Zheng-yi. Sintering boron carbide ceramics without grain growth by plastic deformation as the dominant densification mechanism [J]. Scientific Reports, 2015, 5: 15827.
- [23] YANG H, KIM K. Creep densification behavior of micro and nano metal powder: Grain size-dependent model [J]. Acta Materialia, 2006, 54: 3779–3790.
- [24] DENG Sheng-hua, YUAN Tie-chui, LI Rui-di, ZENG Fan-hao, LIU Guang-hong, ZHOU Xiang. Spark plasma

- sintering of pure tungsten powder: Densification kinetics and grain growth [J]. Powder Technology, 2017, 310: 264–271.
- [25] BERNARD-GRANGER G, GUIZARD C. Spark plasma sintering of a commercially available granulated zirconia powder: I. Sintering path and hypotheses about the mechanism(s) controlling densification [J]. Acta Materialia, 2007, 55: 3493–3504.
- [26] HILLERT M. On the theory of normal and abnormal grain growth [J]. Acta Metallurgica, 1965, 13: 227–238.
- [27] ABZIANIDZE T G, ERISTAVI A M, SHALAMBERIDZE S O. Strength and creep in boron carbide (B₄C) and aluminum dodecaboride (α-AlB₁₂) [J]. Journal of Solid State Chemistry, 2000, 154: 191–193.
- [28] SKOROKHOD V V. Processing, microstructure, and mechanical properties of B₄C-TiB₂ particulate sintered composites. Part II. Fracture and mechanical properties [J]. Powder Metallurgy and Metal Ceramics, 2000, 39: 504-513.
- [29] EBRAHIMI S, HEYDARI M S, BAHARVANDI H R, EHSANI N. Effect of iron on the wetting, sintering ability, and the physical and mechanical properties of boron carbide composites: A review [J]. International Journal of Refractory Metals and Hard Materials, 2016, 57: 78–92.

- [30] ZHANG Mei, LI Rui-di, YUAN Tie-chui, FENG Xiao, XIE Si-yao. Effect of low-melting-point sintering aid on densification mechanisms of boron carbide during spark plasma sintering [J]. Scripta Materialia, 2019, 163: 34–39.
- [31] WEERTMAN J. Theory of stead-state creep based on dislocation climb [J]. Journal of Applied Physics, 1955, 26: 1213–1217.
- [32] UNGÁR T, BORBÉLY A. The effect of dislocation contrast on X-ray line broadening: A new approach to line profile analysis [J]. Applied Physics Letter, 1996, 69: 3173–3175.
- [33] ZHANG Mei, YUAN Tie-chui, DENG Sheng-hua, LI Rui-di, ZHOU Zhi-hui, XU Yun-bao, ZHANG Ying-jie. Novel approach of the evaluation of electric current density during the spark plasma sintering: Effect on the densification mechanisms of B₄C-based ceramics [J]. International Journal of Refractory Metals and Hard Materials, 2022, 102: 105703.
- [34] SANTANACH J G, WEI-EL A, ESTOURNÈS C, YANG Q, LAURENT C, PEIGNEY A. Spark plasma sintering of alumina: Study of parameters, formal sintering analysis and hypotheses on the mechanism(s) involved in densification and grain growth [J]. Acta Materialia, 2011, 59: 1400–1408.

超高温放电等离子烧结碳化硼粉末致密化和晶粒生长动力学

张梅¹, 王文军^{1,2}, 袁铁锤¹, 谢思遥³, 李瑞迪¹, 周志辉¹, 徐运保⁴

- 1. 中南大学 粉末冶金国家重点实验室 轻质高强结构材料重点实验室,长沙 410083;
 - 2. 浙江力博实业股份有限公司,绍兴 312000;
 - 3. 合肥工业大学 材料科学与工程学院, 合肥 230009;
 - 4. 湖南工程学院,湘潭 411100

摘 要:通过放电等离子烧结(SPS)制备致密碳化硼材料,并揭示烧结致密化机制和晶粒生长动力学;研究样品致密度、硬度、抗弯强度和韧性,并通过 SEM 和 TEM 对烧结机制进行验证。结果表明, SPS 碳化硼烧结主要分为两个阶段: 致密化阶段(1800~2000 ℃)和晶粒生长阶段(2100~2200 ℃)。利用稳态蠕变模型进行分析,碳化硼烧结初期致密化机制为晶界滑移,后期转变为位错攀移机制;晶粒生长机制在 2100 ℃时由晶界扩散控制,在 2200 ℃时由体积扩散或液相扩散控制。

关键词:碳化硼;放电等离子烧结;致密化机制;晶粒生长机制;晶界;扩散

(Edited by Bing YANG)